https://doi.org/10.1007/s41230-024-3093-y

Effects of cooling rate on microstructure and microhardness of directionally solidified Galvalume alloy

Ji-peng Li[1], De-gao Qiao[1], Jian Li[1], Xiao-yang Luo[1], *Peng Peng[2], Xian-tao Yan[2], and Xu-dong Zhang[2]

1. Gansu Jiu Steel Group Hongxing Iron and Steel Co., Ltd., Jiayuguan 735111, Gansu, China

2. School of Materials and Energy, Lanzhou University, Lanzhou 730000, China

Abstract: The influences of cooling rate on the phase constitution, microstructural length scale, and microhardness of directionally solidified Galvalume (Zn-55Al-1.6Si) alloy were investigated by directional solidification experiments at different withdrawal speeds (5, 10, 20, 50, 100, 200, and 400 μm·s^{-1}). The results show that the microstructure of directionally solidified Galvalume alloys is composed of primary Al dendrites, Si-rich phase and (Zn-Al-Si) ternary eutectics at the withdrawal speed ranging from 5 to 400 μm·s^{-1}. As the withdrawal speed increases, the segregation of Si element intensifies, resulting in an increase in the area fraction of the Si-rich phase. In addition, the primary Al dendrites show significant refinement with an increase in the withdrawal speed. The relationship between the primary dendrite arm spacing (λ_1) and the thermal parameters of solidification is obtained: $\lambda_1=127.3V^{-0.31}$. Moreover, as the withdrawal speed increases from 5 to 400 μm·s^{-1}, the microhardness of the alloy increases from 90 HV to 151 HV. This is a combined effect of grain refinement and second-phase strengthening.

Keywords: Galvalume alloy; directional solidification; microstructure length scale; microhardness

CLC numbers: TG146.21 **Document code:** A **Article ID:** 1672-6421(2024)03-213-08

1 Introduction

Metal materials possess superior mechanical properties and excellent formability, and are widely used in various fields such as construction, energy, transportation, aerospace, etc [1-2]. However, corrosion susceptibility is a common issue for many traditional metal materials. Corrosion not only deteriorates the strength and durability of metal materials, but also results in waste of energy and resources. As sustainable development and environmental protection attract increasing attention, the global demand of safeguarding metal materials is on the rise. Common anti-corrosion techniques involve alloy modification, surface coating, and electrochemical protection, and so on [3-5].

In the mid-20th century, Borzillo et al. [6] introduced varying amounts of Al and Si into a Zn alloy to investigate the corrosion resistance of the alloy in atmospheric exposure conditions. Subsequently, it was found that the alloy comprised of 55wt.% Al, 43.4wt.% Zn, and 1.6wt.% Si displayed exceptional corrosion resistance, and it was named Galvalume alloy. Moreover, the experimental results indicated that for Al contents below 35wt.%, the corrosion resistance of the alloy slightly decreased as the Al content increases. In the range of 35wt.% to 45wt.% Al, the alloy's corrosion resistance showed a significant proportional increase with an increase in Al content. However, once the Al content exceeded 45wt.%, the alloy's corrosion resistance reached a plateau and remained essentially constant despite further increase in Al content. In additional, the alloy's antioxidant properties were enhanced and the reaction between Al and Fe was inhibited by the addition of Si [7].

In addition to Al and Si elements, the performance of the Galvalume alloy is significantly affected by various other alloying elements, such as Mg, and RE [8-9]. For example, Li et al. [10] conducted a study on the microstructural evolution and corrosion resistance of Zn-55Al-1.6Si alloys with varying Mg contents (0 to 2.5wt.%). The findings revealed the presence of a novel intermetallic phase, $MgZn_2$, within the interdendritic region of the Zn-rich phase. The presence of this intermetallic phase notably enhanced the corrosion

***Peng Peng**

Ph. D., Professor. His research interests mainly focus on the solidification theory of nonferrous alloys (TiAl and Sn-base alloys) during directional solidification, and advanced casting processes of structural superalloys (Ni-base alloys).

E-mail: pengp@lzu.edu.cn

Received: 2023-07-28; Accepted: 2023-11-22

resistance within the interdendritic region. Besides, the introduction of Mg resulted in the formation of a dense and stable corrosion product during the corrosion process of the Zn-55Al-1.6Si-Mg alloy, providing significant protection to the alloy.

Furthermore, studies have demonstrated that addition of rare earth elements (RE) into Zn-Al alloys can significantly decrease the viscosity of the plating solution, thereby enhancing the fluidity of the melt [11-12]. Moreover, the addition of rare earth elements facilitates the removal of impurities and the refinement of the plating layer, thus increasing the coating's corrosion resistance and high temperature durability [13]. This is due to that RE elements can react with impurity elements, such as O and S, at grain boundaries to generate rare earth oxides and sulfides. These compounds serve to strengthen the grain boundaries, consequently mitigating intergranular erosion. Furthermore, as surface-active elements, rare earth elements can reduce the surface tension of the plating solution, leading to a reduction in the critical size for nucleation and enhancing grain refinement [14-15]. Yang et al. [16] studied the effects of La on the corrosion resistance of hot-dip galvanized coatings. They found that with the addition of a certain amount of La in the plating solution, the alloy underwent significant refinement, resulting in a notable improvement in corrosion resistance.

Based on this, researchers rapidly intensified their research efforts on the Galvalume alloy, resulting in the successful development of an array of alloys, including Galfan (Zn-5%Al-Re) and SuperGenius (Zn-11%Al-3%Mg-0.3%Si) [17-18].

As mentioned in previous works, the crystal structure, grain size, and arrangement of grain boundaries have a substantial influence on the mechanical properties, corrosion resistance, as well as various physical and chemical characteristics of an alloy [19]. Therefore, understanding and controlling the microstructure play a vital role in researching and optimizing the performance of Galvalume alloy.

In addition to alloying, the cooling rate also significantly influences the microstructure of alloys [20]. Although previous studies had investigated the effect of cooling rate on the microstructure of Galvalume alloy, quantitative and qualitative research on the microstructure and phase distribution of the alloy under various cooling rates is still limited. Therefore, it is imperative to undertake additional research on the influence of cooling rate on the microstructure of Galvalume alloy, which presents a great challenge. It is worth noting that directional solidification technology can accurately control the cooling rate, which is crucial for studying the solidification behavior of alloys.

This study aims to examine the solidification behavior of Galvalume alloy under varying cooling rates by employing directional solidification technology. The phase constitution, microstructural characteristic length scales, and microhardness of the Galvalume alloy directionally solidified at different withdrawal speeds were obtained. Additionally, the impact of cooling rate on the microstructure and mechanical properties of the alloy was explored.

2 Experimental procedures

2.1 Sample preparation

The as-cast Galvalume alloy (Zn-55Al-1.6Si) ingot was obtained through the melting of pure Zn and Al-Si intermediate alloy in a resistance furnace, followed by air cooling. The test rods of 7 mm in diameter and 100 mm in length were fabricated from the ingot. The directional solidification experiments were conducted in a Bridgman-type furnace, as depicted in Fig. 1. The specimen was heated to 600 °C in an Al_2O_3 ceramic tube and held for 30 min to achieve homogeneous melting of the alloy. Subsequently, the specimens were immersed into liquid Ga-In-Sn alloy at different solidification velocities: 5, 10, 20, 50, 100, 200, and 400 μm·s^{-1}, respectively. The growth distance was set at 30 mm. Temperature measurement was conducted using two thermocouples installed in the DS furnace, and the temperature gradient near the solid/liquid interface was recorded as 30 K·mm^{-1}. The entire experiment was conducted under a high-purity argon gas atmosphere.

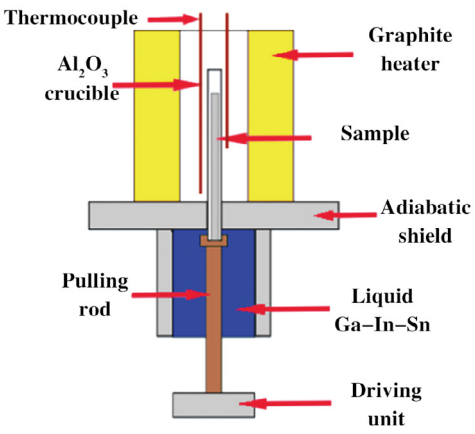

Fig. 1: Schematic of the Bridgman-type directional solidification apparatus

2.2 Characterization methods

The samples were sectioned along parallel and perpendicular growth directions to analyze the microstructure of the steady-state growth region. The phase constitution of the alloy was analyzed using the X-ray diffraction (Rigaku D/MAX-2400) with a Cu-Kα radiation operating at 40 kV and 30 mA. Scans were performed at a scanning speed of 4°·min^{-1} within the 2θ range of 10°–90°. The microstructure of the alloy was studied using scanning electron microscopy (SEM; Apreo-s) equipped with an energy-dispersive X-ray spectrometer (EDS). Grain size and dendrite spacing were quantified by the professional image analysis software, Image-J. The primary dendrite arm spacing (λ_1) was obtained using a linear intercept method in the longitudinal section of the samples. The microhardness of the samples was measured using a Vickers hardness tester (Wilson VH1102) with a load of 50 gf and a holding time of 30 s. To make sure the accuracy of the results, at least 5 measurements were conducted, and the mean value was taken as the result.

3 Results and discussion

3.1 Microstructure of as-cast Zn-55Al-1.6Si alloy

The Galvalume alloy (Zn-55Al-1.6Si) is a hypereutectic Zn-Al alloy that deviates significantly from the eutectic composition [21]. The SEM micrograph of as-cast Galvalume alloy is shown in Fig. 2. The microstructure predominantly consists of large dendrites and fibrous eutectic structures. In addition, needle-like and irregular precipitates are observed interlaced within the dendritic structure. Based on the EDS analysis results shown in Fig. 3 and the XRD results presented in Fig. 4, it can be inferred that the dendritic phase is primary Al dendrite, the eutectic region corresponds to the Al-Zn-Si ternary eutectic, and the needle-like and irregular precipitates are rich in Si. Furthermore, it is evident that Si is present in all phases, indicating a significant segregation of Si during solidification.

According to the ternary phase diagram of the Al-Zn-Si system, at 525 °C, the Zn-55Al-1.6Si alloy is located in the two-phase region of the Al and liquid phase [22]. After solidification of Al phase, the composition of the remaining liquid phase moves towards the ternary eutectic point. Since Zn is much more soluble in Al than Si, the composition of the remaining liquid phase deviates from the ternary eutectic point [23]. In this case, the binary eutectic reaction occurs, forming a mixture of Al and Si. The liquid phase components continue to move towards the ternary eutectic point. After reaching the ternary eutectic point, the remaining liquid phase undergoes a ternary eutectic reaction to form a ternary eutectic product of Zn, Al and Si.

3.2 Microstructure of directionally solidified Zn-55Al-1.6Si alloys

Figure 4 shows the XRD diffraction patterns of the as-cast and directionally solidified Galvalume alloys under various withdrawal speeds. All the diffraction peaks corresponding to Al, Zn, and Si phase are observed, suggesting that the phase constitution of the alloy remains unchanged with increasing withdrawal speed. At lower withdrawal speeds, the grains with smaller deviations from the optimal orientation have a greater

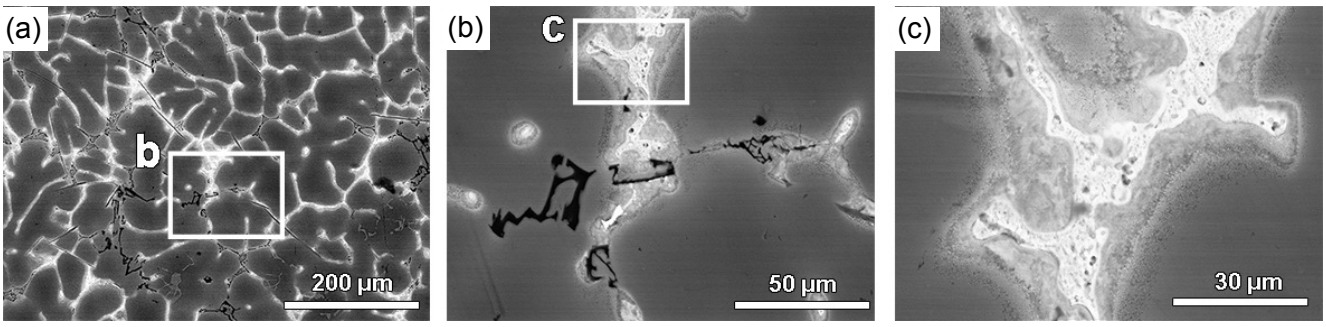

Fig. 2: Microstructure of as-cast Galvalume alloy: (a) SEM image; (b)–(c) magnified local views of image

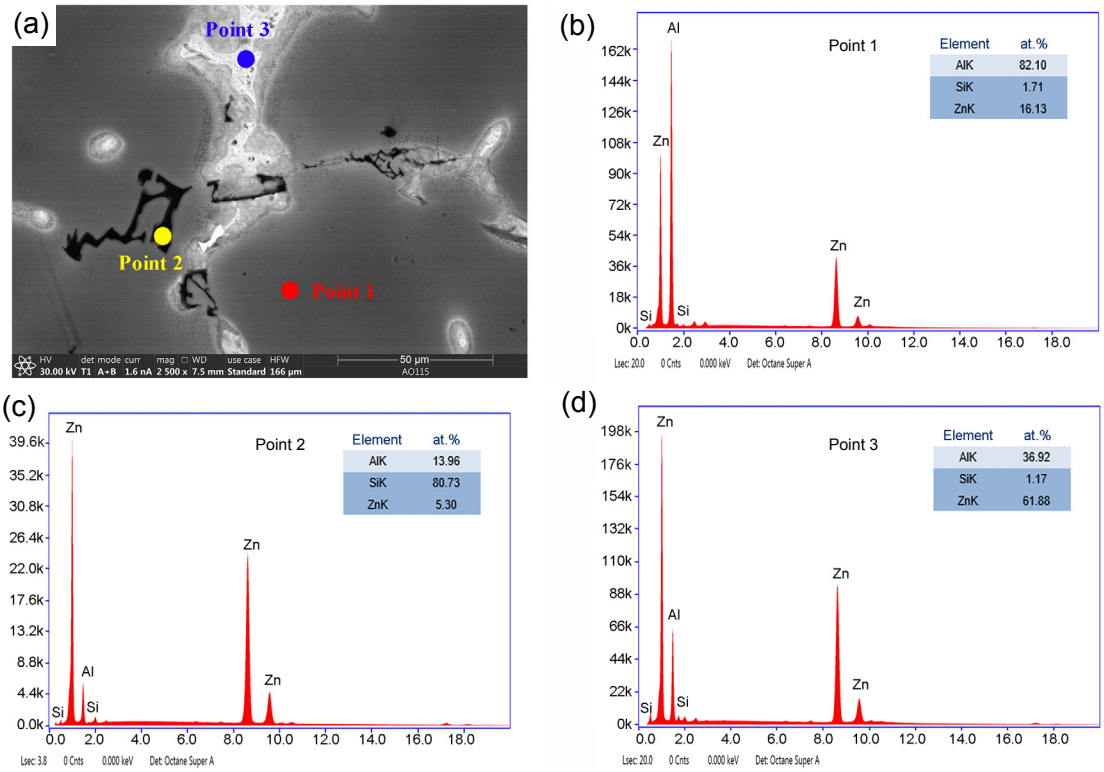

Fig. 3: EDS results of as-cast galvalume alloy: (a) microstructure; (b to d) EDS results of Points 1 to 3 in (a)

vertical velocity, grow faster, dominating the growth process. As the withdrawal speed increases, the growth dominance of these grains becomes weaker and the grains with different orientations grow along the direction parallel to the heat flow, as shown by

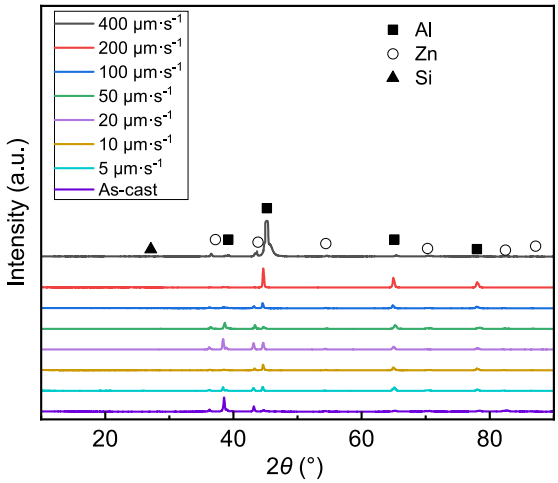

Fig. 4: XRD results of directionally solidified Galvalume alloys at different withdrawal speeds

the significant increase in the intensity of the peaks in specific orientation (200) with higher withdrawal speed. In addition, with the increase of the withdrawal rate, the diffraction peaks of the Al phase shift to a higher angle. This can be attributed to the fact that the size of Si atoms is much smaller than that of Al atoms, Si element exists in the Al phase as an interstitial solid solution. With the increase of the withdrawal speed, the precipitation of Si elements increases, the solid solubility of Si in the Al phase decreases, and the lattice distortion of Al phase decreases, resulting in a decrease in the lattice parameter and a shift of the diffraction peaks to a higher angle.

Figure 5 shows the steady-state microstructures of the transversal sections of the directionally solidified Galvalume alloys at different withdrawal speeds (V=5, 10, 20, 50, 100, 200, 400 μm·s^{-1}). Combined with the EDS results for as-cast sample and XRD results for samples after directional solidification, the phase constitution of the samples after directional solidification is consistent with the as-cast alloy, consisting of primary Al dendrites, Zn-Al-Si ternary eutectic, and Si phase. With the increase in withdrawal speed, the area fraction of the Si-rich

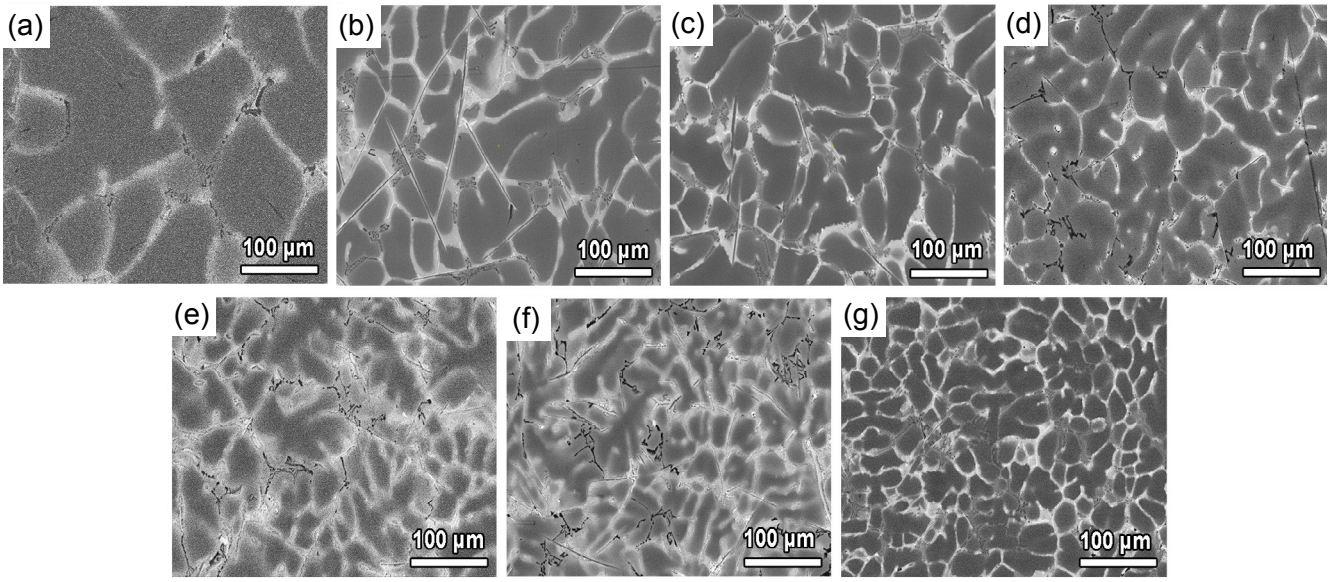

Fig. 5: SEM images on transverse section of directionally solidified Galvalume alloys at different withdrawal speeds: (a) 5 μm·s^{-1}; (b) 10 μm·s^{-1}; (c) 20 μm·s^{-1}; (d) 50 μm·s^{-1}; (e) 100 μm·s^{-1}; (f) 200 μm·s^{-1}; (g) 400 μm·s^{-1}

phase exhibits a continuous increasing trend (Fig. 6). Moreover, as the withdrawal speed increases, the grains in the stable growth zone are effectively refined. This is due to the fact that at lower withdrawal speeds, the grains have sufficient time to grow during solidification, resulting in the formation of larger grains. Furthermore, with the increase of withdrawal speed, the composition undercooling of the melt at the solid-liquid interface increases, which promotes the nucleation of a great number of primary Al and Al-Si eutectic grains, leading to grain refinement [24]. Simultaneously, the accelerated withdrawal speed reduces the diffusion and exacerbates the segregation of alloying elements. Thus, Si element aggregates at grain boundaries and more Si-rich phases are formed.

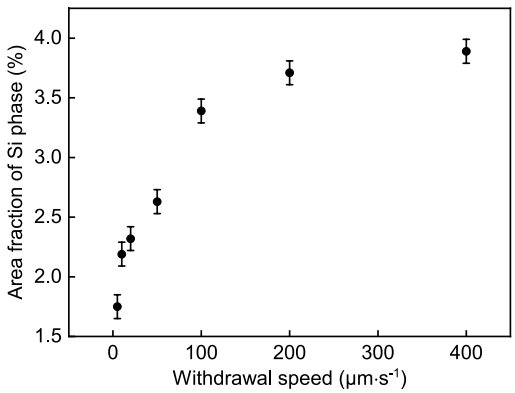

Fig. 6: Relationship between area fraction of Si phase and withdrawal speed

Figure 7 illustrates the steady-state microstructures of longitudinal sections of directionally solidified Galvalume alloys at different withdrawal speeds (V=5, 10, 20, 50, 100, 200, 400 μm·s^{-1}). It can be observed that the direction of the primary dendrite is parallel to the direction of the heat flow. As shown in Figs. 7(a–c), the primary Al phase exhibits a clear cellular structure at withdrawal speeds of 5, 10, and 20 μm·s^{-1}. With a further increase in the withdrawal speed to over 50 μm·s^{-1}, the primary Al phase displays a distinct regular arrangement of secondary dendrites.

At slower withdrawal speeds, the reduced composition undercooling at the solid-liquid interface enables the grains to preserve a cellular columnar structure. However, with an increase in withdrawal speed, the equilibrium diffusion of solute at the solid-liquid interface is disrupted [25]. As a result, the columnar crystals establish a new equilibrium by decreasing the tip radius, which enhances the expulsion of the solute, intensifying the composition undercooling at the solid-liquid interface, and ultimately promoting the nucleation and growth of secondary dendrites [26].

Figure 8 presents the solid-liquid interface morphologies of the directionally solidified Galvalume alloys at different withdrawal speeds. In the withdrawal speed range of 5 μm·s^{-1} to 400 μm·s^{-1}, the solidification interface shows characteristics of dendrites. Compared with steady-state microstructures shown in Fig. 7, it can be observed that when the withdrawal speeds are 5, 10, and 20 μm·s^{-1}, the primary Al phase transforms from cellular morphology to dendritic during the solidification process. This is due to that the expulsion of solutes in the solidification process changes the solid-liquid interface of the melt composition, leading to the final destabilization of the solidification interface and the formation of primary Al dendrites.

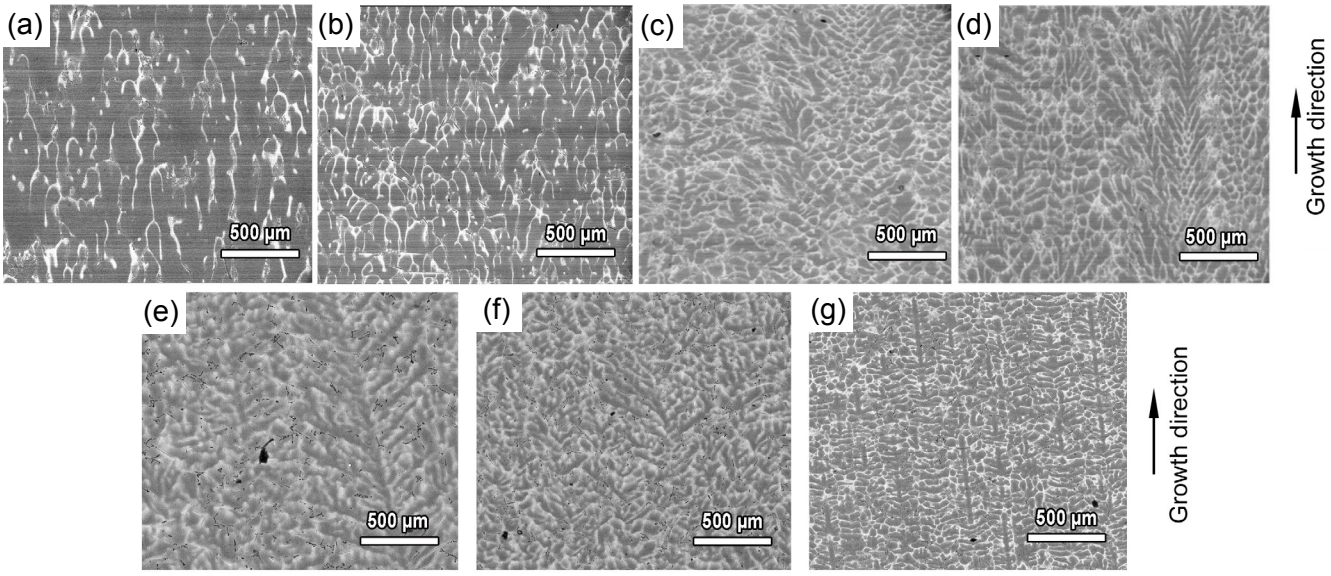

Fig. 7: Steady-state longitudinal microstructures of directionally solidified Galvalume alloys at different withdrawal speeds: (a) 5 μm·s^{-1}; (b) 10 μm·s^{-1}; (c) 20 μm·s^{-1}; (d) 50 μm·s^{-1}; (e) 100 μm·s^{-1}; (f) 200 μm·s^{-1}; (g) 400 μm·s^{-1}

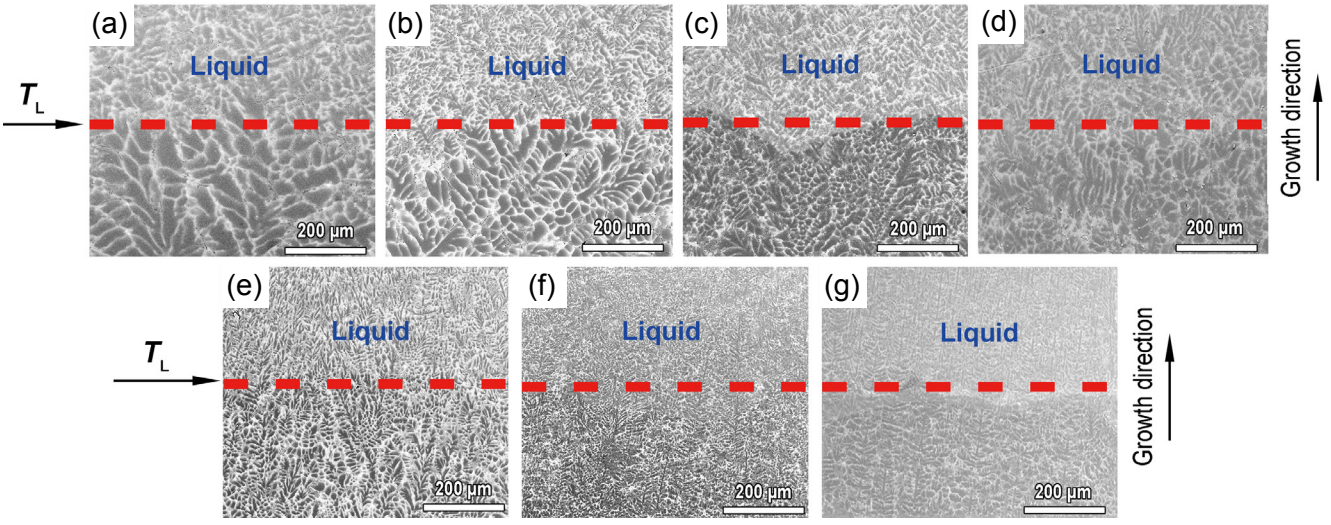

Fig. 8: Solid-liquid interface morphologies of directionally solidified Galvalume alloys at different withdrawal speeds: (a) 5 μm·s^{-1}; (b) 10 μm·s^{-1}; (c) 20 μm·s^{-1}; (d) 50 μm·s^{-1}; (e) 100 μm·s^{-1}; (f) 200 μm·s^{-1}; (g) 400 μm·s^{-1}

3.3 Effect of withdrawal speed on dendrite arm spacing of Galvalume alloy

Figure 9 shows the statistics of primary cellular/dendrite arm spacing at different withdrawal speeds. It can be seen that the primary dendrite arm spacing decreases with the increase of the withdrawal speed. At a withdrawal speed of 5 μm·s^{-1}, the primary dendrite arm spacing is 105 μm; while at a withdrawal speed of 400 μm·s^{-1}, the primary dendrite arm spacing is reduced to 24 μm. The dendrite arm spacings are determined by the heat dissipation conditions at the solidification interface [27]. During directional solidification, rapid solidification enhances the heat dissipation at the solid-liquid interface. The latent heat of crystallisation released during solidification in the dendrites dissipates quickly in the solid phase and has a lower impact on the remaining liquid phase, leading to a decrease in dendrite arm spacing. Trivedi et al. [28] developed the dendrite growth model based on the Hunt model [29] and Marginal Stability criterion [30], as shown in Eq. (1):

$$\lambda_1 = 2.83\left[m(k-1)D\Gamma L\right]^{0.25} C_0^{\ 0.25} G_L^{\ -0.5} V^{-0.25} \quad (1)$$

where λ_1 is the primary dendrite arm spacing, m is liquidus slope, k is partition coefficient, D is solute diffusivity, C_0 is the actual composition of the alloy, Γ is Gibbs-Thomson coefficient, G_L is temperature gradient in liquid, and L is the constant associated with disturbances. It can be seen that in the case of a constant composition, λ_1 is only related to the temperature gradient at the solid-liquid interface (G_L) and the withdrawal speed (V).

Neglecting the effect of growth rate on the temperature gradient, the Trivedi model can therefore be simplified as follows:

$$\lambda_1 = KV^{-0.25} \quad (2)$$

where K is a constant related to alloy characteristics and solidification parameters.

Based on the measurement results illustrated in Fig. 9, the fitting curve is as follows:

$$\lambda_1 = 127.3V^{-0.31} \quad (3)$$

As shown in Fig. 9, the tendency of experimental results are consistent with the Trivedi model. The primary dendrite arm spacing shows a significant dependence on the withdrawal speed. At lower withdrawal speeds, λ_1 is more susceptible to the effect of growth rate, whereas at higher withdrawal speeds, the effect of withdrawal speed on dendrite arm spacing is not obvious. This is a combined effect of dendrite nucleation and solute diffusion [31].

3.4 Effect of withdrawal speed on microhardness of Galvalume alloy

The Vickers hardness and hardness indentation of directionally solidified alloys at different withdrawal speeds are presented in Figs. 10 and 11, respectively. It can been seen in Fig. 10 that the microhardness of as-cast Galvalume alloy is 108 HV. At the withdrawal speed of 5 μm·s^{-1}, the microhardness of directionally solidified sample is 90 HV, and as the withdrawal speed increases to 400 μm·s^{-1}, the microhardness increases to 151 HV.

As shown in Fig. 11, with the increase of withdrawal speed, the primary Al dendrite is significantly refined. With finer grains, the alloy has a greater number of grains and grain boundaries. When neighboring grains of different orientations are deformed by force, the dislocations within the grain with a large Schmidt factor starts at first and slips along a certain crystal plane [32]. Whereas the dislocations' slipping to the grain boundaries is hindered, the aggregation of dislocations within the grain boundaries is generated, preventing further movement of the dislocations, thus increasing the strength and hardness of the alloy.

Furthermore, besides the primary Al phase, the Si phase exists in the alloy. It has been proved that the harder and more numerous the second phase, the greater the hardness strengthening effect on the alloy [33]. Si is a hard and brittle phase, which is distributed on the grain boundaries in the form of a network, and is much harder than Zn and Al phases. The area fraction of the Si phase increases continuously with the withdrawal speed, causing the microhardness of the alloy to increase as well. Therefore, the enhanced microhardness of the alloy is a synergistic effect of grain refinement and second phase strengthening.

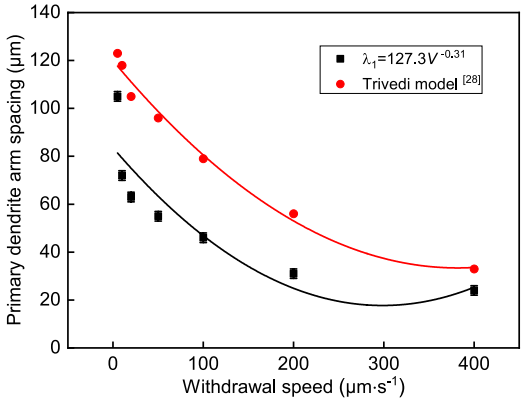

Fig. 9: Variations of primary dendrite arm spacing with withdrawal speed

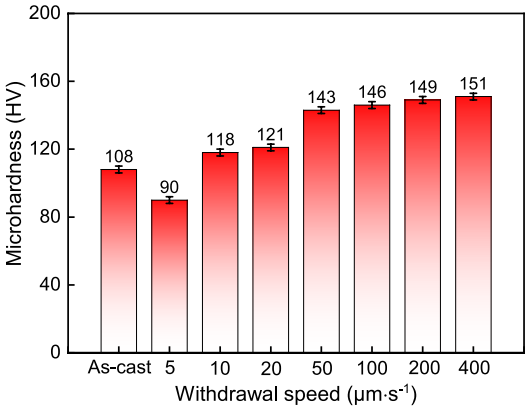

Fig. 10: Relationship between microhardness and withdrawal speed of the alloys

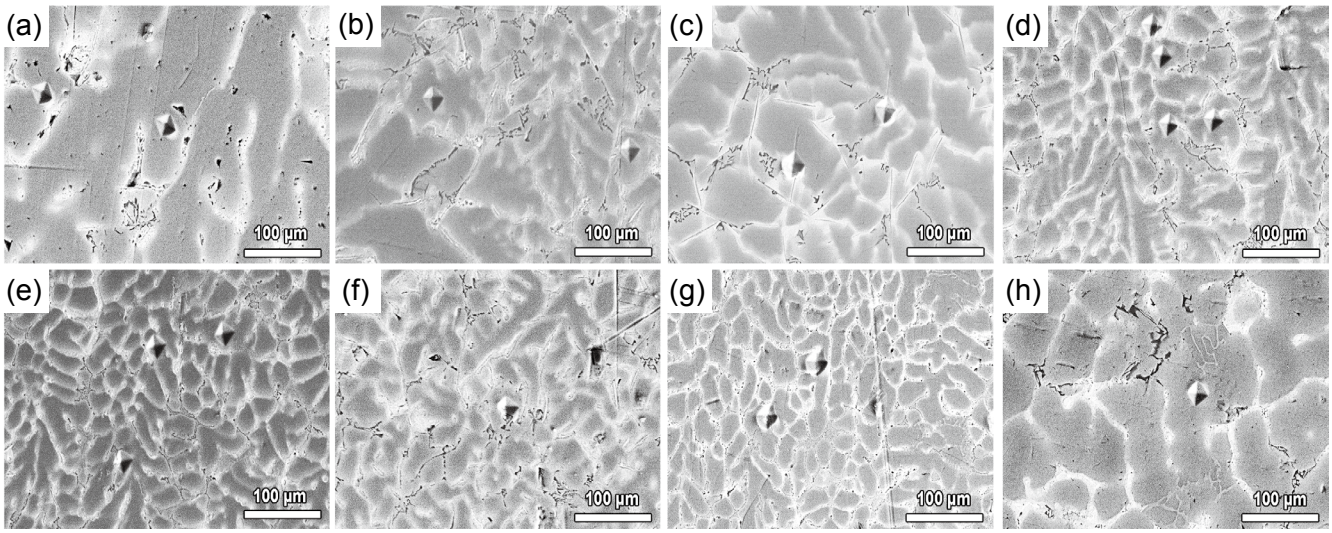

Fig. 11: Hardness indentation of directionally solidified alloys at different withdrawal speeds: (a) 5 μm·s^{-1}; (b) 10 μm·s^{-1}; (c) 20 μm·s^{-1}; (d) 50 μm·s^{-1}; (e) 100 μm·s^{-1}; (f) 200 μm·s^{-1}; (g) 400 μm·s^{-1}; (h) as-cast

4 Conclusions

In this work, the microstructure and microhardness of directionally solidified Galvalume (Zn-55Al-1.6Si) alloy under different withdrawal speeds were investigated. Following conclusions are obtained:

(1) The Galvalume alloy directionally solidified under different withdrawal speeds (5, 10, 20, 50, 100, 200, and 400 μm·s^{-1}) are composed of primary Al dendrites, Si-rich phase and (Zn-Al-Si) ternary eutectic. The increasing withdrawal speed enhances the segregation of the Si-rich phase.

(2) With an increase in the withdrawal speed, the Al dendrites show significant refinement. The relationship between the primary dendrite arm spacing of directionally solidified Galvalume alloy and withdrawal speed is obtained: $\lambda_1=127.3V^{-0.31}$.

(3) The microhardness of the Galvalume alloy increases significantly with an increase in withdrawal speed, which is attributed to the combined effects of grain refinement and second phase strengthening.

Acknowledgments

This study was financially supported by the Key Science and Technology Projects of Gansu Province (Grant No. 22ZD6GB019), Gansu Key Research and Development Project (Grant No. 23YFGA0003), Gansu Provincial Joint Research Fund (Grant No. 23JRRC0004), Fundamental Research Funds for the Central Universities (Grant No. lzujbky-2022-ey15), and the State Key Laboratory of Solidification Processing in NPU (Grant No. SKLSP202204).

Conflict of interest

The authors declare that they have no conflict of interest.

References

[1] Livatyali H, Duggal N, Ahmetoglu A, et al. Investigation of crack formation on the galvalume coating of roll formed roof panels. Materials Processes Technology, 2000, 98: 53–61.
[2] Pritzel A, Manhabosco S M, Rodrigues J S. Comparative study of the corrosion behavior of galvanized, galvannealed and Zn-55Al coated interstitial free steels. Surface and Coatings Technology, 2015, 279: 150–160.
[3] Wu Z, Sandlöbes S, Wu L, et al. Mechanical behaviour of Zn-Al-Cu-Mg alloys: Deformation mechanisms of as-cast microstructures. Materials Science and Engineering: A, 2016, 651: 675–687.
[4] Shibli S M A, Meena B N, Remya R. A review on recent approaches in the field of hot dip zinc galvanizing process. Surface and Coatings Technology, 2015, 262: 210–215.
[5] Sandoval-Jimenez A, Negrete J, Torres-Villasenor G. Phase transformations in the Zn-Al eutectoid alloy after quenching from the high temperature triclinic beta phase. Materials Characterization, 2010, 61(11): 1286–1289.
[6] Borzillo A R, Crowley J E, Horton J B. Non-ferrous metal coated products and method of production thereof. Bethlehem Steel Corporation, Patent No. CA899729A, 1972.
[7] Guo T X, Liu C S, Ran C R. Effects of spangle size on performances of hot-dip 55%Al-Zn alloy coating. International Journal of Electrochemical Science, 2018, 13(10): 9505–9519.
[8] Qiu P, Leygraf C, Wallinder I O. Evolution of corrosion products and metal release from Galvalume coatings on steel during short and long-term atmospheric exposures. Materials Chemistry and Physics, 2012, 133(1): 419–428.
[9] Xu J, Gu Q F, Li Q, et al. Influence of Ti and La additions on the formation of intermetallic compounds in the Al-Zn-Si bath. Metallurgical and Materials Transactions A, 2016, 47: 6542–6554.
[10] Li S, Gao B, Tu G, et al. Effects of magnesium on the microstructure and corrosion resistance of Zn-55Al-1.6Si coating. Constructure and Building Materials, 2014, 71: 124–131.
[11] Chuvil'deev N V, Nokhrin A V, Kopylov V I, et al. Investigation of mechanical properties and corrosion resistance of fine-grained aluminum alloys Al-Zn with reduced zinc content. Journal of Alloys and Compounds, 2022, 891: 162110.
[12] Ho C Y, Wang J Y. Investigation of microstructure related to corrosion evolution, mechanical and electrochemical properties on doped Si of binary Zn-Al coating. Materials Chemistry and Physics, 2023, 301: 127656.

[13] Mohammad W U, Torbjörn C. Silicon crystal morphologies during solidification refining from Al-Si melts. Journal of Crystal Growth, 2011, 318(1): 212–218.
[14] Peng H P, Su X P, Li Z, et al. Synergistic effect of Cu and Si on hot-dipping galvalume coating. Surface and Coatings Technology, 2012, 206(21): 4329–4334.
[15] Bi G L, Luo X M, Jiang J, et al. Effect of Zn, Cu and Ni addition on microstructure and mechanical properties of as-cast Mg-Dy alloys. China Foundry, 2016, 13(1): 54–58.
[16] Yang D, Chen J S, Han Q, et al. Effects of lanthanum addition on corrosion resistance of hot-dipped galvalume coating. Journal of Rare Earths, 2009, 27(1): 114–118.
[17] Rudimylla S, Cássio A P, Silva T A. Hypereutectic Zn-Al alloys: Microstructural development under unsteady-state solidification conditions, eutectic coupled zone and hardness. Metals, 2022, 12: 1076.
[18] Albert G, Walter A. General method of phase analysis for individual multicomponent alloys. Metallurgical and Materials Transactions: B, 1970, 1: 2551–2556.
[19] Liu C, Su Y Q, Bi W S. Phase and its morphologies of Ti-45% Al alloy directionally solidified at different growth rates. Transactions of Nonferrous Metals Society of China, 2005, 15(2): 286–290.
[20] Peng P, Li S Y, Chen W Q. Phase selection and mechanical properties of directionally solidified AlCoCrFeNi2.1 eutectic high-entropy alloy. Journal of Alloys and Compounds, 2022, 898: 162907.
[21] Chen S L, Chang Y A. A thermodynamic analysis of the Al-Zn system and phase diagram calculation. Calphad, 1993, 17(2): 113–124.
[22] Talita A, Crystopher B, Thiago S, et al. Near-eutectic Zn-Mg alloys: Interrelations of solidification thermal parameters, microstructure length scale and tensile/corrosion properties. Materials Chemistry Physics, 2019, 19: 582–598.
[23] Shanmukha K A, Kamanio C, Abhik C. Exotic three-phase microstructures in the ternary Ag-Cu-Sb eutectic system. Acta Materialia, 2021, 221: 117400.
[24] Zhang X, Leygraf C, Wallinder I O. Atmospheric corrosion of galfan coatings on steel in chloride-rich environments. Corrosion Science, 2013, 73: 62–71.
[25] Garcıá F, Salinas A, Nava E. The role of Si and Ti additions on the formation of the alloy layer at the interface of hot-dip Al-Zn coatings on steel strips. Materials Letter, 2006, 60: 775–778.
[26] Jiang L, Volovitch P, Wolpers M. Activation and inhibition of Zn-Al and Zn-Al-Mg coatings on steel by nitrate in phosphoric acid solution. Corrosion Science, 2012, 60(7): 256–264.
[27] Feng K, Huang X F, Ma Y, et al. Microstructure evolution of ZA72 magnesium alloy during partial remelting. China Foundry, 2013, 10(2): 74–80.
[28] Trivedi R, Kurz W. Dendritic growth. International Materials Reviews, 1994, 39(2): 49–74.
[29] Hunt J D. Solidification and casting of metals. London: The Metal Society, 1979.
[30] Mullins W W, Sekerka R F. Stability of a planar interface during solidification of a dilute binary alloy. Journal of Applied Physics, 1996, 35: 323–329
[31] Ezemenaka D, Patino C, Genau A. Microstructural evolution in directionally solidified Al-Cu-Mg ternary eutectic. Journal of Alloys and Compounds, 2021, 883: 160818
[32] Smudde C M, San C W, Hill M R, et al. Evaluation of residual stress reproducibility and orientation dependent fatigue crack growth in powder bed fusion stainless steel. Materials Science and Engineering: A, 2023, 879: 145266.
[33] Yang C A, Li B S, Ren M X, et al. Gypsum bonded investment for micro-structure casting of $ZnAl_4$. China Foundry, 2010, 7(3): 270–274.